Mercury fluxes from hydrothermal venting at mid-ocean ridges constrained by measurements

Natalia Torres-Rodriguez, Jingjing Yuan, Sven Petersen, Aurélie Dufour, David González-Santana, Valérie Chavagnac, Hélène Planquette, Milena Horvat, David Amouroux, Cécile Cathalot, et al.

nature geoscience

Article

https://doi.org/10.1038/s41561-023-01341-w

Mercury fluxes from hydrothermal venting at mid-ocean ridges constrained by measurements

Received: 4 April 2023

Accepted: 25 October 2023

Published online: 12 December 2023

Check for updates

Natalia Torres-Rodriguez[1] ✉, Jingjing Yuan[2], Sven Petersen[3], Aurélie Dufour[1], David González-Santana[4], Valérie Chavagnac[5], Hélène Planquette[6], Milena Horvat[7], David Amouroux[8], Cécile Cathalot[9], Ewan Pelleter[9], Ruoyu Sun[2], Jeroen E. Sonke[5], George W. Luther III[10] & Lars-Eric Heimbürger-Boavida[1] ✉

Methylmercury is a potent toxin threatening the global population mainly through the consumption of marine fish. Hydrothermal venting directly delivers natural mercury to the ocean, yet its global flux remains poorly constrained. To determine the extent to which anthropogenic inputs have increased oceanic mercury levels, it is crucial to estimate natural mercury levels. Here we combine observations of vent fluids, plume waters, seawater and rock samples to quantify the release of mercury from the Trans-Atlantic Geotraverse hydrothermal vent at the Mid-Atlantic Ridge. The majority (67–95%) of the mercury enriched in the vent fluids (4,966 ± 497 pmol l^{-1}) is rapidly diluted to reach background seawater levels (0.80 pmol l^{-1}). A small Hg fraction (2.6–10%) is scavenged to the Trans-Atlantic Geotraverse mound rocks. Scaling up our findings and previous work, we propose a mercury flux estimate of 1.5–64.7 t per year from mid-ocean ridges. This hydrothermal flux is small in comparison to anthropogenic inputs. This suggests that most of the mercury present in the ocean must be of anthropogenic origin and that the implementation of emissions reduction measures outlined in the Minamata Convention could effectively reduce mercury levels in the global ocean and subsequently in marine fish.

Methylmercury (MeHg) is a potent toxin that poses a threat to marine life and human health[1], with expected global economic losses of US$19 trillion by 2050[2]. The United Nations Minamata Convention on Mercury (Hg) aims to reduce human exposure to Hg by reducing anthropogenic emissions. Decades of research have comprehensively quantified recent global anthropogenic Hg emissions to 3,100 t per year (ref. 3). It is believed that anthropogenic Hg emissions have increased surface ocean Hg levels threefold since pre-industrial times[4]. Yet, to quantify

[1]Aix Marseille Université, CNRS/INSU, Université de Toulon, IRD, Mediterranean Institute of Oceanography (MIO), Marseille, France. [2]Institute of Surface-Earth System Science, School of Earth System Science, Tianjin University, Tianjin, China. [3]GEOMAR-Helmholtz Centre for Ocean Research, Kiel, Germany. [4]Fundación Canaria Parque Científico Tecnológico de la Universidad de las Palmas de Gran Canaria, Las Palmas de Gran Canaria, Spain. [5]Géosciences Environment Toulouse GET CNRS UMR5563, IRD/UPS/CNES, Université de Toulouse, Toulouse, France. [6]CNRS, IRD, Ifremer, LEMAR, University of Brest, Plouzané, France. [7]Jozef Stefan Institute, Department of Environmental Sciences, Ljubljana, Slovenia. [8]Université de Pau et des Pays de l'Adour, E2S UPPA, CNRS, IPREM, Institut des Sciences Analytiques et de Physico-chimie pour l'Environment et les Matériaux, Pau, France. [9]UMR6538 Geo-Ocean, IFREMER CNRS UBO UBS, Plouzané, France. [10]School of Marine Science and Policy, University of Delaware, Lewes, DE, USA.
✉e-mail: natalia.torres-rodriguez@mio.osupytheas.fr; lars-eric.heimburger@mio.osupytheas.fr

how much anthropogenic Hg emissions have increased oceanic Hg levels, natural Hg inputs must be constrained. Atmospheric deposition, riverine inputs and submarine groundwater discharge are secondary Hg sources that recycle natural and anthropogenic Hg to the ocean. Hydrothermal vents release natural Hg into the ocean. Over 80% of the active volcanoes worldwide are oceanic[5], yet their associated hydrothermal Hg fluxes remain poorly constrained. Indirect assessments via mass balance considerations proposed hydrothermal Hg fluxes between 360 and 3,720 t per year (refs. 6–8). The 2018 Global Mercury Assessment lowered the hydrothermal Hg flux from 600 t per year in the 2013 assessment to 100 t per year (ref. 3). Fluxes of Hg range from 20 to 2,000 t per year when scaling up direct hydrothermal vent fluid measurements from the four available studies at deep sites[9]. Total mercury (tHg) concentrations of the vent fluids used for this estimate range from 5 to 11,000 pmol l^{-1} (refs. 10–13).

Less is known about the fate of Hg in hydrothermal plumes when hydrothermal fluids mix with seawater, partially because early measurements of Hg in seawater near plumes were erroneous[14,15]. Two GEOTRACES transect cruises, crossing the slow-spreading Mid-Atlantic Ridge (MAR) and the fast-spreading East Pacific Rise, investigated Hg in hydrothermal plumes[16,17]. One sample above their seawater background levels (median 0.89 pmol l^{-1}; Extended Data Table 1) with a Hg concentration of 13 pmol l^{-1} was reported at the MAR[17]. No change in Hg distributions was observed in the large plume of the East Pacific Rise[16]. Here we combine hydrothermal vent fluids, plume waters and rock samples from the Trans-Atlantic Geotraverse hydrothermal field (TAG) of the MAR to assess the fate of hydrothermal Hg inputs. We then use our findings to provide a refined estimate of hydrothermal Hg flux from mid-ocean ridges to the global ocean.

Mercury release from TAG hydrothermal vent site

We collected hydrothermal vent fluids, plume waters and seawater surrounding TAG on three dedicated oceanographic cruises. The unfiltered tHg concentrations of the vent fluid samples were 4,206 ± 262, 2,968 ± 87 and 367 ± 18 pmol l^{-1}. During hydrothermal venting, magnesium (Mg) is quantitatively removed from seawater by precipitation as magnesium-hydroxy-sulfate hydrate. We used magnesium (Mg) concentrations of the vent fluid samples (4.59 ± 0.046, 32.9 ± 0.329 and 48.1 ± 0.481 mmol l^{-1}) and their respective tHg concentrations to extrapolate the Mg-free vent fluid end member to 4,966 ± 497 pmol l^{-1} (Extended Data Fig. 1)[18]. The good correlation between tHg and Mg (R^2 = 0.91) suggests that the tHg variations in the measured vent fluids are mainly due to mixing with surrounding seawater, with contributions from a single vent or fluid type. Previous studies at deep hydrothermal sites reported vent fluid tHg concentrations ranging from 5 to 11,000 pmol l^{-1} (refs. 10–13). Differences in geological settings may account for the variation in tHg concentrations of vent fluids. However, the vent fluid end member tHg concentration was not calculated in previous studies so different degrees of mixing with seawater may also explain the variability. The calculated vent fluid end member is around 6,000 times enriched in tHg compared with the median tHg concentration of the Atlantic Ocean (0.80 ± 0.42 pmol l^{-1}; n = 1,917; Extended Data Fig. 2 and Extended Data Table 1).

Seawater and plume waters were collected during the HERMINE cruise (GEOTRACES GApr07) following the TAG plume flow dispersion in the water column. The tHg concentrations vary from 0.28 to 2.03 pmol l^{-1}. The tHg concentrations are homogeneous from the surface to the deep waters at all stations (Fig. 1). In general, hot, acidic, low-density vent fluids are expelled through hydrothermal chimneys in buoyant plumes that rise in the water column mixing with seawater. Once the density of the buoyant plumes equals the density of seawater, the plumes reach neutral buoyancy and start moving laterally in non-buoyant plumes[19]. Non-buoyant plumes have been followed up to thousands of kilometres away from vent sites[20,21]. In this study, the definition of the magnitude and extent of the buoyant and non-buoyant plume was based on potential temperature, salinity, potential density and nephelometry (suspended matter) (grey shading in Fig. 1). The highest tHg concentration (2.03 pmol l^{-1}) is observed within the buoyant plume layer at the TAG vent site (Fig. 1). High tHg concentrations (around 1 pmol l^{-1}) are evident in the non-buoyant layer up to 10 km from the vent site (Fig. 1). The median of all the tHg values of this study including seawater and plume waters is 0.63 ± 0.077 pmol l^{-1} (n = 195) (Extended Data Table 1), a value slightly lower than the median of 0.80 pmol l^{-1} of the entire Atlantic Ocean, and in the range of 0.53–0.89 pmol l^{-1} reported for the North Atlantic Ocean where TAG is located (Extended Data Table 1)[17,22]. Concentrations of MeHg are low in the surface waters (0.05 pmol l^{-1} average above 500 m depth, n = 25), a peak around 1,000 m depth and consistently high concentrations at depth (0.28 pmol l^{-1} average below 1,000 m depth, n = 155) (Fig. 1). All plume waters and seawater samples display MeHg concentrations within previously reported range for the Atlantic Ocean (Extended Data Fig. 2 and Extended Data Table 1). Despite the high tHg concentration of the vent fluid end member, there is no detectable tHg or MeHg enrichment in the nearby waters (median tHg of 0.63 ± 0.077 pmol l^{-1} and median MeHg of 0.19 ± 0.12 pmol l^{-1}). This may suggest that MeHg hydrothermal inputs at TAG are low, nor do the hydrothermal inputs stimulate MeHg production locally.

Dilution vs scavenging

Elements released from the hydrothermal vents can be diluted in seawater or scavenged onto sinking particles[23]. We used dissolved manganese (dMn) as an index to assess the importance of Hg removal processes following venting. Owing to its slow oxidation rate, dMn has been used as a conservative tracer of the dilution of vent fluids along hydrothermal plumes. During the cruise transit, particulate manganese (pMn) was lower than dMn with concentrations consistent with oceanic background levels[24] (Extended Data Fig. 3). Average pMn considering all stations and depths within the plume was 2.5% of the total manganese (tMn) (Extended Data Fig. 4). Following previous studies[19,25,26], we thus use dMn as a conservative tracer along the plume, being affected only by dilution. Combining manganese (Mn) data of the plume with our previously reported Mn concentration of the vent fluid end member at TAG (0.43 mmol l^{-1}) (ref. 27), we calculate the dilution factor from the vent fluid end member to the non-buoyant plume (equation (1) and Extended Data Fig. 5). For comparison, dilution factors were calculated separately using tMn and dMn concentrations in the plume. No substantial difference was found between the two approaches, thus in further discussions, we refer to the dilution factor calculated with dMn (Extended Data Fig. 5). The average calculated dilution factor considering all depths with the plume and stations is $2.79 \times 10^5 \pm 1.4 \times 10^3$. The dilution factor is 2.36×10^4 at the TAG vent site and increases with distance to reach 1.21×10^6 at station 9 located 10 km away (Extended Data Fig. 5). Dilution factors are rather similar within the non-buoyant plume at each station.

To determine the relative importance of dilution and scavenging as the main process controlling the distribution of tHg, the estimated dilution factor was used to calculate expected tHg concentrations along our plume transect (C_n in equation (2)). Expected concentration (C_n) is the concentration that would be observed if only dilution drives changes in concentrations in the plume. Calculations were made using the Atlantic Ocean tHg median (0.80 pmol l^{-1}; Extended Data Fig. 2 and Extended Data Table 1) and the tHg values reported in this study for the vent fluid end member and the plume waters (Extended Data Fig. 1 and Fig. 1). If measured tHg concentrations are equal to those expected (dilution efficiency = 100%; equation (3)), then tHg is behaving conservatively so that dilution is responsible for all the tHg losses from the vent to the plume. If observed tHg concentrations are below the expected ones (dilution efficiency < 100%), dilution cannot account for all the losses from the plume. Occasional dilution efficiencies above 100% may suggest that Hg is behaving more conservatively than

https://doi.org/10.1038/s41561-023-01341-w

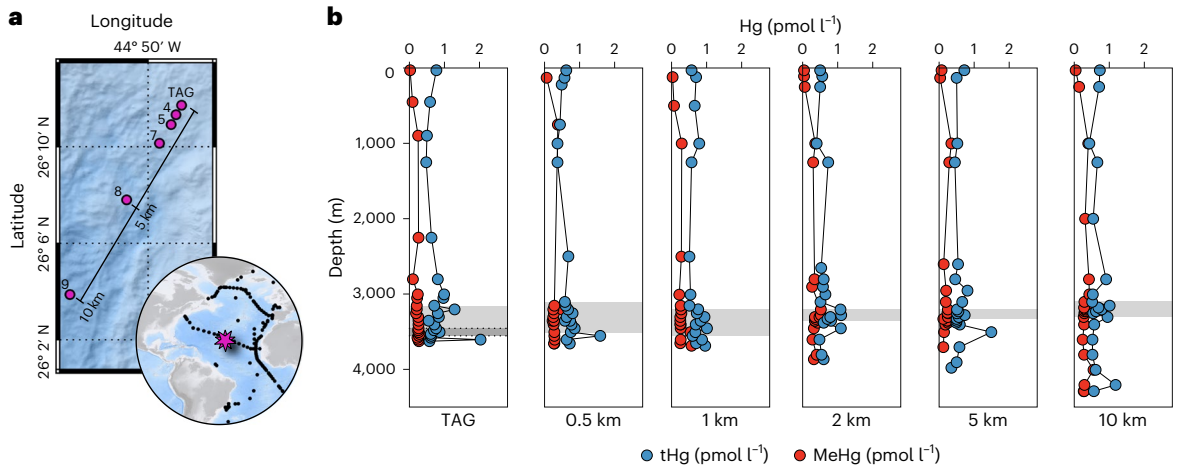

Fig. 1 | Location of the TAG hydrothermal vent site sampled stations and vertical profiles for tHg and MeHg. a, Location of the TAG vent site (pink star), seawater literature data (black circles) and sampled stations (pink circles). Bathymetry from cruise M127 GEOMAR. **b**, tHg and MeHg vertical profiles. The grey shading shows the non-buoyant plume layer. Dotted lines and darker grey shading at the TAG station bound the depths of the buoyant plume. Maps in **a** created with QGIS (https://qgis.org/en/site).

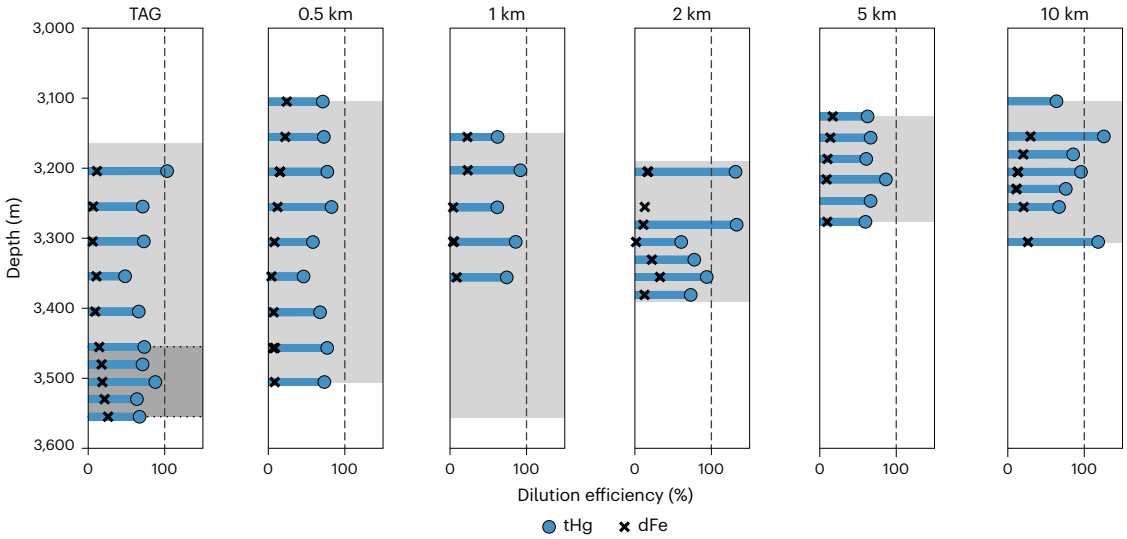

Fig. 2 | Dilution efficiency at different stations and depths. Blue shows tHg dilution efficiency. Black crosses indicate dFe dilution efficiency. The grey shading shows the non-buoyant plume depth. Dotted lines and darker shading at the TAG station bound the depths of the buoyant plume.

dMn. Mean tHg dilution efficiencies per station range from 67 to 95% (Fig. 2). At the TAG station, the tHg mean dilution efficiency is 72%. The tHg dilution efficiencies tend to increase as the distance from the vent site increases, reaching 90% 10 km from the vent. Considering all plume depths and all stations, the dilution efficiency is 73 ± 20%, suggesting that tHg is largely conservative at TAG. Assuming that only dilution and scavenging account for losses from the plume, scavenging would remove the remaining 27% tHg.

To assess the validity of the dilution model, the dilution efficiency of dFe and tFe were also calculated. Calculations were made using the average seawater dFe (0.70 nmol l^{-1}) (ref. 28), our previously reported Fe concentrations of the vent fluid end member (5.4 mmol l^{-1}) (ref. 27) and plume Fe values[19] (Extended Data Fig. 3). The average dilution efficiency considering all stations and depths within the plume is 14 ± 7% for dFe (Fig. 2) and 39 ± 8% for tFe (Extended Data Fig. 6). These low dFe and tFe dilution efficiencies are in good agreement with the previously reported non-conservative behaviour of Fe at TAG[19,23].

Although Hg dilution efficiencies are relatively high, there is still potentially substantial deposition of Hg near the vent field. To further corroborate our observations, we analysed surface rocks and drill-core samples. The lithology of the active mound can be divided into six layers (Fig. 3a). The uppermost layer (Fe oxyhydroxides and cherts) displays Hg concentrations varying from 74 to 409 ng g^{-1} with a median of 112 ± 145 ng g^{-1} (circles in Fig. 3) and includes typical supergene lithologies including red ochres, Fe oxides, Mn-Fe oxyhydroxides and sulfides with different degrees of alteration (Extended Data Table 2). The massive sulfide layer displays concentrations from 99.9 to 1,187 ng g^{-1} when all the samples found in the layer are considered (Fig. 3 and Extended Data Table 3) but between 949 and 1,187 ng g^{-1} with a median of 1,021 ± 122 ng g^{-1} if just the typical massive sulfide samples (massive pyrite; Extended Data Table 3) are considered. The remaining layers, including anhydrite-rich, pyrite-silica, silicified wallrock breccias and chloritized basalt breccias, referred to as the stockwork zone, display Hg concentrations from 50 to 331 ng g^{-1} with a median of

https://doi.org/10.1038/s41561-023-01341-w

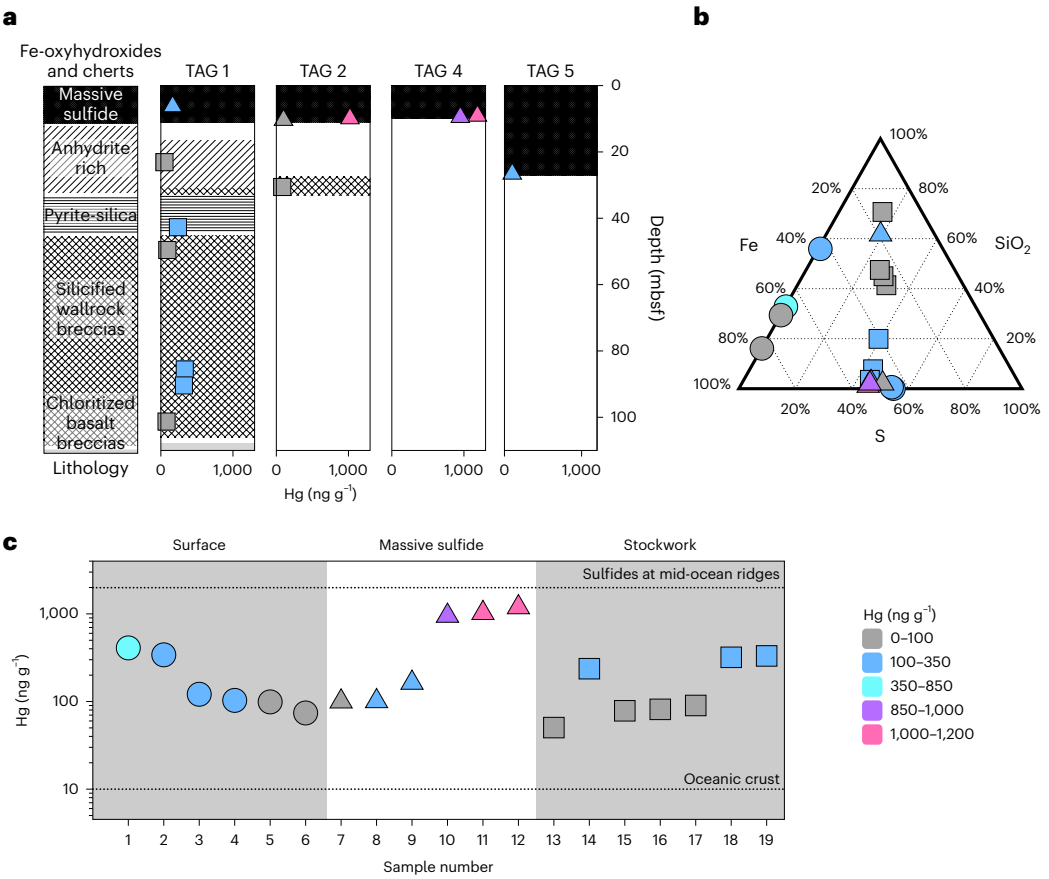

Fig. 3 | Hg concentrations of surface rock and drill-core samples. a, Lithology of the TAG mound deposit with the six layers and Hg concentrations of the drill-core samples. The depth of the drill-core samples is given in metres below the seafloor (mbsf). **b**, Ternary Fe-S-SiO_2 diagram with all the rock samples. **c**, Hg concentrations of the rock samples from the surface, massive sulfide and stockwork layers. The numbers in the horizontal axis indicate the number of the sample as in Extended Data Tables 2 and 3. The black dotted lines indicate the Hg concentration of the oceanic crust[30] and the median Hg concentration of hydrothermal sulfides at mid-ocean ridges[31]. Circles denote surface samples, triangles show samples from the massive sulfide layer and squares show samples from the stockwork zone. Note that the Hg concentrations are shown in a colour scheme.

90 ± 123 ng g^{-1}. Hydrothermal sulfides (samples that lie in the bottom centre of the ternary diagram in Fig. 3b) show the highest Hg concentrations. The Hg concentrations are lower in silica-rich samples (upper part of the ternary diagram in Fig. 3b). This partitioning is due to the affinity of Hg for iron and sulfide phases rather than quartz, anhydrite or altered minerals in the host rock[29]. All samples display Hg enrichments in comparison to the typical oceanic crust concentrations[30], with the surface and stockwork samples enriched up to ten times and the massive sulfide layer samples up to 100 times (Fig. 3c). The Hg concentrations of the typical massive sulfides recovered from TAG (purple and pink triangles in Fig. 3c) are within the range reported for other mid-ocean ridge areas (mean 1,991 ng g^{-1}, $n = 1{,}026$)[31].

The best volume estimate of the TAG deposit is 2.95×10^6 t of rock at the active site, with 2.27×10^6 t in the massive sulfide layer and 6.8×10^5 t in the stockwork zone[32]. Using the median Hg concentrations measured for each layer (1,021 ng g^{-1} for the massive sulfide layer and 90 ng g^{-1} for the stockwork zone), the Hg in the deposit is estimated to be 2.38 t, with 2.32 t of Hg accumulated in the massive sulfide layer and 0.06 t Hg in the stockwork zone (part 1, Extended Data Table 4). Hydrothermal heat flux at TAG's active mound was monitored during a seven-month interval, with a heat output varying from 55 to 86 MW (ref. 33). Older estimates present heat fluxes of up to 225 MW for the active portion of TAG[34]. Using the minimum and maximum heat flux estimates (55 and 225 MW), the volume flux of the discharged hydrothermal fluid at TAG is calculated to 0.04–0.14 m^3 s^{-1} (equation (4), part 2, Extended Data Table 4)[33,35,36]. On the basis of the tHg concentration of the vent fluid end member (4,966 ± 497 pmol l^{-1}) and the volume flux estimate, the discharge of tHg from the active TAG mound is estimated between 1,113 to 4,553 g per year (part 2, Extended Data Table 4). The activity at TAG has been proposed to occur on an intermittent basis, with 20,000 years of activity in the last 50,000 years of history[37]. The tHg release from TAG in all the active history of the site can be estimated between 22 and 91 t (part 3, Extended Data Table 4). If we consider that from the calculated 22 to 91 t of Hg that have been released from TAG in all the active history of the site, a minor fraction of 2.38 t (2.6–10%) has been retained in the deposit and that calculations indicate that dilution alone can explain the distribution of Hg from the vent to the plume (tHg dilution efficiency considering all the depths within the plume and all stations is around 73%; Fig. 2). We conclude with independent lines of evidence that Hg behaves conservatively at TAG. Thus, Hg released from TAG is able to persist long enough in the deep ocean and thereby contribute to the global Hg cycle (Fig. 4).

Implications for the global Hg cycle

We attempt to scale up our results by combining our findings with information from previous works to provide a measurements' based estimate of hydrothermal Hg inputs. Submarine hydrothermal vents occur at tectonic plate boundaries including mid-ocean ridges, back-arc basins and submarine volcanic arcs. Hydrothermal sulfides from arc volcanoes display higher Hg concentrations than rocks from other

https://doi.org/10.1038/s41561-023-01341-w

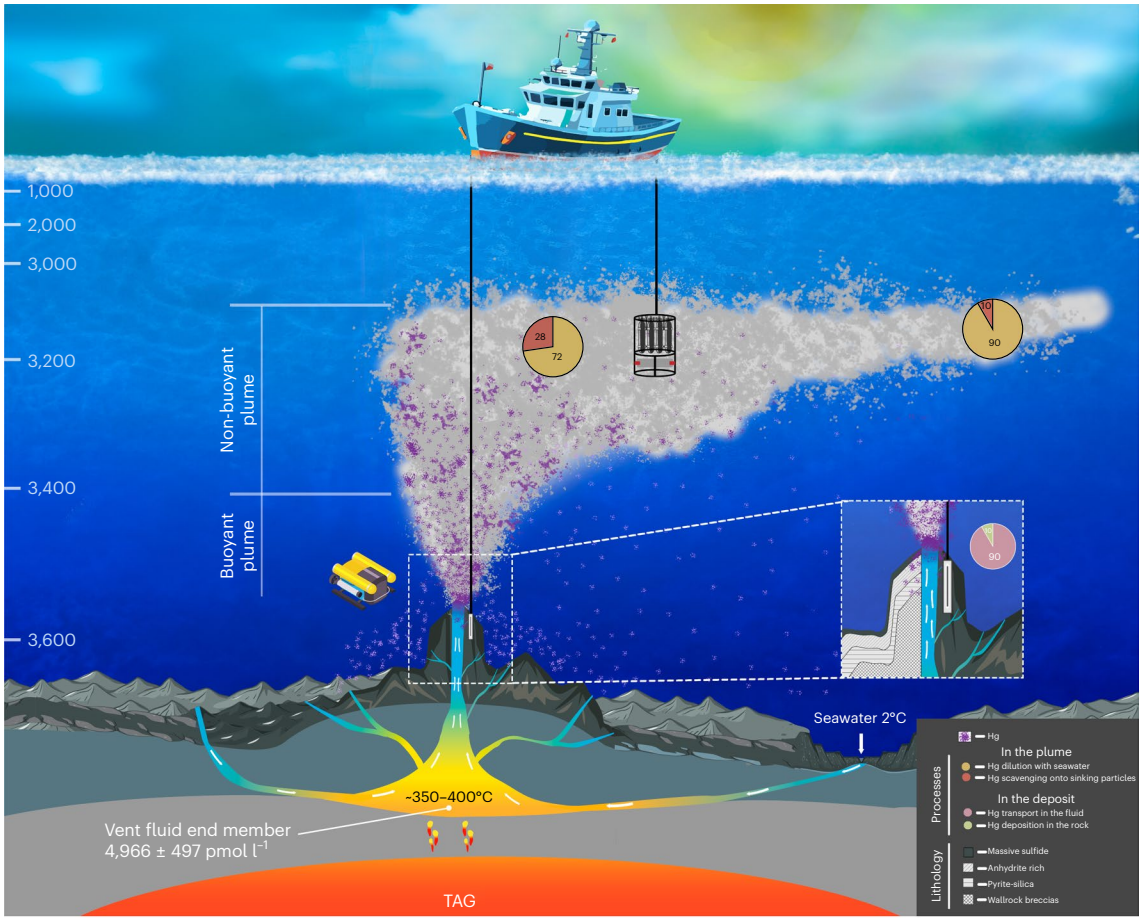

Fig. 4 | Schematic model of Hg inputs at TAG. Seawater percolates the oceanic crust and is heated up reaching its maximum temperature close to the magma source. The vent fluid end member ascends through the hydrothermal vent where 10% of the Hg precipitates and stays in the rock. As the vent fluid is released from the vent, it starts mixing with seawater. Dilution with seawater accounts for most of the Hg losses from the plume with a maximum of 28% scavenging onto sinking particles at the TAG station.

tectonic settings (36,000 ng g^{-1}, $n = 241$)[31]. Higher Hg concentrations at arc volcanoes may be attributed to sediment inputs during subduction and the subsequent release of magmatic volatiles into the hydrothermal systems. Back-arc settings and arc volcanoes can also occur at shallower depths than mid-ocean ridges. Shallow hydrothermal systems at arc volcanoes and back-arc regions generally release fluids of lower temperature and a higher volatile fraction, driving different Hg inputs[9]. Given these geological constraints, we use our results from TAG to provide an estimate for mid-ocean ridges exclusively. We use the latest global high-temperature mid-ocean ridge water flux estimate of (0.17–2.93) × 10^{13} kg per year (ref. 38) and the vent fluid tHg concentration of TAG (4,966 ± 497 pmol l^{-1}) to calculate a mid-ocean ridge hydrothermal Hg flux between 1.5 and 32.1 t per year (part 4, Extended Data Table 4). Given that the highest tHg concentration of vent fluids reported at mid-ocean ridges is 11,000 pmol l^{-1} (ref. 10), the upper limit of the Hg hydrothermal flux estimate can be expanded to 64.7 t per year.

Recent models estimate that the annual Hg inputs to the oceans are 4,300–7,800 t per year from atmospheric deposition[39] and 893–1,224 t per year from riverine discharge[40], making a total of 5,193–9,024 t per year. The terrestrial natural volcanic and crustal degassing Hg inputs into the atmosphere have recently been revised to 335 ± 100 t per year (ref. 41). These natural terrestrial emissions are partly deposited in the ocean and partly in soils. Soil Hg can be sequestered for decades to centuries before running off via rivers to the oceans. Therefore, the anthropogenic inputs to the ocean can be calculated by subtracting the natural terrestrial flux (335 ± 100 t per year) from the total Hg input (5,193–9,024 t per year), resulting in 4,755–8,789 t per year (part 5, Extended Data Table 4). Given that mid-ocean ridges host the majority of known and projected hydrothermal vents, it is likely that they account for the majority of the global hydrothermal Hg flux[42]. Therefore, the flux of natural Hg to the ocean can be calculated as the sum of the terrestrial natural flux (335 ± 100 t per year) and the estimated mid-ocean ridge hydrothermal flux (1.5–65 t per year) to 237–500 t per year (part 5, Extended Data Table 4). The natural Hg flux to the ocean is therefore equivalent to 3–11% of the anthropogenic Hg flux to the ocean. The Minamata Convention on Mercury aims to reduce human exposure to Hg by reducing anthropogenic Hg emissions. As modern oceanic Hg levels seem to be predominantly due to anthropogenic inputs, we anticipate that the implementation of strict anti-pollution policies will lead to an effective reduction of oceanic Hg levels. Future research should focus on hydrothermal Hg inputs from arc volcanoes, back-arc settings, eruptive volcanism and off-axis venting to further constrain the global hydrothermal Hg flux to the ocean.

Online content

Any methods, additional references, Nature Portfolio reporting summaries, source data, extended data, supplementary information, acknowledgements, peer review information; details of author contributions and competing interests; and statements of data and code availability are available at https://doi.org/10.1038/s41561-023-01341-w.

References

1. UNEP *Global Mercury Assessment 2018* (UN Environment Programme, Chemicals and Health Branch, 2018).
2. Zhang, Y. et al. Global health effects of future atmospheric mercury emissions. *Nat. Commun.* **12**, 3035 (2021).
3. Outridge, P. M., Mason, R. P., Wang, F., Guerrero, S. & Heimbürger-Boavida, L. E. Updated global and oceanic mercury budgets for the United Nations Global Mercury assessment 2018. *Environ. Sci. Technol.* **52**, 11466–11477 (2018).
4. Lamborg, C. H. et al. A global ocean inventory of anthropogenic mercury based on water column measurements. *Nature* **512**, 65–68 (2014).
5. Sigurdsson, H. In *Encyclopedia of Volcanoes* (eds Sigurdsson, H. et al.) 271–279 (Academic Press, 2000).
6. Fitzgerald, W. F., Engstrom, D. R., Mason, R. P. & Nater, E. A. The case for atmospheric mercury contamination in remote areas. *Environ. Sci. Technol.* **32**, 1–7 (1998).
7. Fitzgerald, W. F. & Lamborg, C. H. *Treatise on Geochemistry* 2nd edn, 91–129 (Elsevier, 2014).
8. Rasmussen, P. E. Current methods of estimating atmospheric mercury fluxes in remote areas. *Environ. Sci. Technol.* **28**, 2233–2241 (1994).
9. German, C. R. et al. Hydrothermal impacts on trace element and isotope ocean biogeochemistry. *Philos. Trans. A Math. Phys. Eng. Sci.* **374**, 20160035 (2016).
10. Crespo-Medina, M. et al. Adaptation of chemosynthetic microorganisms to elevated mercury concentrations in deep-sea hydrothermal vents. *Limnol. Oceanogr.* **54**, 41–49 (2009).
11. Lee, S. et al. Mercury accumulation in hydrothermal vent mollusks from the southern Tonga Arc, southwestern Pacific Ocean. *Chemosphere* **127**, 246–253 (2015).
12. Lamborg, C. H., Damm, K. L. V., Fitzgerald, W. F., Hammerschmidt, C. R. & Zierenberg, R. Mercury and monomethylmercury in fluids from Sea Cliff submarine hydrothermal field, Gorda Ridge. *Geophys. Res. Lett.* **33**, 17 (2006).
13. Sherman, L. S. et al. Mercury isotopic composition of hydrothermal systems in the Yellowstone Plateau volcanic field and Guaymas Basin sea-floor rift. *Earth Planet Sci. Lett.* **279**, 86–96 (2009).
14. Carr, R. A., Jones, M. M. & Russ, E. R. Anomalous mercury in near-bottom water of a Mid-Atlantic Rift valley. *Nature* **251**, 489–490 (1974).
15. Carr, R. A., Jones, M. M., Warner, T. B., Cheek, C. H. & Russ, E. R. Variation in time of mercury anomalies at the Mid-Atlantic Ridge. *Nature* **258**, 588–589 (1975).
16. Bowman, K. L., Hammerschmidt, C. R., Lamborg, C. H., Swarr, G. J. & Agather, A. M. Distribution of mercury species across a zonal section of the eastern tropical South Pacific Ocean (U.S. GEOTRACES GP16). *Mar. Chem.* **186**, 156–166 (2016).
17. Bowman, K. L., Hammerschmidt, C. R., Lamborg, C. H. & Swarr, G. Mercury in the North Atlantic Ocean: the U.S. GEOTRACES zonal and meridional sections. *Deep Sea Res. Part II* **116**, 251–261 (2015).
18. Edmond, J. M., Damm, K. L. V., McDuff, R. E., & Measures, C. I. Chemistry of hot springs on the East Pacific Rise and their effluent dispersal. *Nature* **297**, 187–191 (1982).
19. González-Santana, D. et al. Processes driving iron and manganese dispersal from the TAG hydrothermal plume (Mid-Atlantic Ridge): results from a GEOTRACES process study. *Front. Mar. Sci.* **7**, 568 (2020).
20. Resing, J. A. et al. Basin-scale transport of hydrothermal dissolved metals across the South Pacific Ocean. *Nature* **523**, 200–203 (2015).
21. Wu, J., Wells, M. L. & Rember, R. Dissolved iron anomaly in the deep tropical–subtropical Pacific: evidence for long-range transport of hydrothermal iron. *Geochim. Cosmochim. Acta* **75**, 460–468 (2011).
22. Cossa, D. et al. Mercury distribution and transport in the North Atlantic Ocean along the Geotraces-GA01 transect. *Biogeosciences* **15**, 2309–2323 (2018).
23. German, C. R., Campbell, A. C. & Edmond, J. M. Hydrothermal scavenging at the Mid-Atlantic Ridge: modification of trace element dissolved fluxes. *Earth Planet Sci. Lett.* **107**, 101–114 (1991).
24. Cheize, M. et al. High resolution particulate trace metals dispersion from the TAG hydrothermal vent (Mid-Atlantic Ridge). *Goldschmidt Abstr.* 376 (2018).
25. Field, M. P. & Sherrell, R. M. Dissolved and particulate Fe in a hydrothermal plume at 9° 45′ N, East Pacific Rise: slow Fe (II) oxidation kinetics in Pacific plumes. *Geochim. Cosmochim. Acta* **64**, 619–628 (2000).
26. Wang, H. et al. Iron ligands and isotopes in hydrothermal plumes over backarc volcanoes in the Northeast Lau Basin, Southwest Pacific Ocean. *Geochim. Cosmochim. Acta* https://doi.org/10.1016/j.gca.2022.09.026 (2022).
27. Findlay, A. J., Gartman, A., Shaw, T. J. & Luther, G. W. Trace metal concentration and partitioning in the first 1.5 m of hydrothermal vent plumes along the Mid-Atlantic Ridge: TAG, Snakepit, and Rainbow. *Chem. Geol.* **412**, 117–131 (2015).
28. Hatta, M. et al. An overview of dissolved Fe and Mn distributions during the 2010–2011 U.S. GEOTRACES north Atlantic cruises: GEOTRACES GA03. *Deep Sea Res. Part II* **116**, 117–129 (2015).
29. Lim, D., Kim, H., Kim, J., Jeong, D. & Kim, D. Mercury proxy for hydrothermal and submarine volcanic activities in the sediment cores of Central Indian Ridge. *Mar. Pollut. Bull.* **159**, 111513 (2020).
30. McDonough, W. F. & Sun, S.-s The composition of the Earth. *Chem. Geol.* **120**, 223–253 (1995).
31. Monecke, T., Petersen, S., Hannington, M. D., Grant, H. & Samson, I. M. in *The Minor Element Endowment of Modern Sea-floor Massive Sulfide Deposits and Comparison with Deposits Hosted in Ancient Volcanic Successions* (eds Verplanck, P. L. & Hitzmanvol. M. W) 18, 245–306 (Society of Economic Geologists, 2016).
32. Graber, S. et al. Structural control, evolution, and accumulation rates of massive sulfides in the TAG hydrothermal field. *Geochem. Geophys. Geosyst.* **21**, 9 (2020).
33. Goto, S., Kinoshita, M., Schultz, A. & Herzen, R. P. V. Estimate of heat flux and its temporal variation at the TAG hydrothermal mound, Mid-Atlantic Ridge 26° N. *J. Geophys. Res. Solid Earth* **108**, B9 (2003).
34. Rona, P. A. et al. Active and relict sea-floor hydrothermal mineralization at the TAG hydrothermal field, Mid-Atlantic Ridge. *Econ. Geol.* **88**, 1989–2017 (1993).
35. Fischer, H. B., List, E. J., Koh, R. C. Y., Imberger, J. & Brooks, N. H. *Mixing in Inland and Coastal Waters* (Academic Press, 1979).
36. Turner, J. S. & Campbell, I. H. Temperature, density and buoyancy fluxes in "black smoker" plumes, and the criterion for buoyancy reversal. *Earth Planet Sci. Lett.* **86**, 85–92 (1987).
37. Lalou, C. et al. New age data for Mid-Atlantic Ridge hydrothermal sites: TAG and Snakepit chronology revisited. *J. Geophys. Res. Solid Earth* **98**, 9705–9713 (1993).
38. Nielsen, S. G. et al. Hydrothermal fluid fluxes calculated from the isotopic mass balance of thallium in the ocean crust. *Earth Planet Sci. Lett.* **251**, 120–133 (2006).
39. Sonke, J. E. et al. Global change effects on biogeochemical mercury cycling. *Ambio* https://doi.org/10.1007/s13280-023-01855-y (2023).
40. Liu, M. et al. Rivers as the largest source of mercury to coastal oceans worldwide. *Nat. Geosci.* **14**, 672–677 (2021).
41. Li, C. et al. Unequal anthropogenic enrichment of mercury in Earth's Northern and Southern hemispheres. *ACS Earth Space Chem.* **4**, 2073–2081 (2020).

42. Beaulieu, S. E., Baker, E. T. & German, C. R. Where are the undiscovered hydrothermal vents on oceanic spreading ridges? *Deep Sea Res. Part II* **121**, 202–212 (2015).

Methods

Samples from TAG, located at 26° 80′ N, 44° 50′ W and 3,620 m depth, were collected during three different oceanographic cruises. Vent fluids were sampled in 2012 during the SNAPMORE cruise onboard the R/V *Knorr*. Seawater and hydrothermal plume fluids were collected in 2017 during the HERMINE cruise (labelled GEOTRACES GApr07) cruise onboard the French R/V *Pourquoi Pas?*. Rock and drill-core samples were recovered in 1994 during the Ocean Drilling Program leg 158.

Sample collection

High-temperature hydrothermal vent fluids were collected unfiltered into gas-tight titanium samplers using the Remotely Operated Vehicle Jason II. Three samples for tHg from the vent fluids were collected and subsampled into 40 ml glass vials. All glassware used was acid cleaned with 3% v/v double-distilled HCl, rinsed with ultrapure water (18 MΩ cm, MilliQ), dried under a flow hood and then muffled at 450 °C for 4 hours. Surface rock samples (Extended Data Table 2) were collected by a series of dives of the submersible Alvin to the TAG active mound. Drill-core samples (Extended Data Table 4) are from drilling sites TAG1, TAG2, TAG4 and TAG5. As all the drilling sites are located in the active 200 m diameter TAG black smoker complex, all drilling locations are considered one site. More than one drill core was done at each location to recover as much stratigraphic section as possible. Cores were described and subsampled onboard. Rock samples were ground and homogenized with an agate mortar before Hg analyses. Seawater and plume waters were sampled by means of a trace metal clean carousel consisting of a polyurethane powder-coated aluminium frame attached to a Kevlar line. A conductivity temperature depth sensor (CTD, Seabird 911plus) was mounted on the trace metal clean rosette, and suspended matter data were processed in real time. The direction of the plume was monitored by a Lowered Acoustic Doppler Current Profiler deployed on a CTD/rosette before each trace metal clean cast. The trace metal clean carousel was equipped with 24 Teflon-lined 12 l GOFLO bottles with external closing. In total, 195 samples for tHg were collected unfiltered into 40 ml glass vials (Brooks Rand Instruments). For MeHg, 192 samples were collected unfiltered into 155 ml polyethylene terephthalate bottles (VWR) and acidified to 0.4% v/v with ultrapure trace metal clean HCl. All samples were stored at 4 °C until analysis.

Measurements

The tHg concentrations were measured within six months of sampling by a single gold trap custom-made purge and trap system[43] following the US Environmental Protection Agency Method 1631. The vent fluid samples were vortexed before 1 ml was subsampled into 60 ml glass vials. To ensure the release of all Hg in the particles, 2 ml inverse aqua regia (VHCl/VHNO3 = ½) was added to the subsample. The subsamples were capped with a glass marble and heated to 120 °C for 8 hours. Recovery was evaluated using the reference material NIST-3133 (National Institute of Standards and Technology) (recovery > 99%) and blanks were run in ultrapure water (18 MΩ cm, MilliQ). The titanium syringe, used for vent fluid sampling, was blank tested by adding a background seawater sample. One subsample was taken a few minutes after adding the seawater to the syringe and a second the day after. The blank was determined to be 4.4 ± 1.9 pmol l^{-1} equivalent to less than 1% of the lowest vent fluid concentration measured in this study. For the seawater samples, oxidation was done using a BrCl solution. Potassium bromide (Sigma-Aldrich) and potassium bromate (Sigma-Aldrich) were heated for 4 h at 250 °C to remove Hg traces before preparing the BrCl solution with double-distilled HCl. A standard addition protocol was used to blank test the BrCl before adding it to the samples. Known volumes of BrCl were added to the same seawater sample, and the Hg concentration was measured. Increasing concentrations of Hg with the increasing volume of added BrCl would imply contamination of the BrCl solution. No contamination was found. After oxidation of the vent fluids and seawater, tHg was measured by cold vapour atomic fluorescence. To calibrate the tHg measurements, a seven-point calibration curve was constructed ($R^2 > 0.9998$) spiking the reference material NIST-3133 into previously purged Hg-free seawater. Standard bracketing with NIST was done every six samples as a quality control to correct for the instrumental drift. The recovery was 94 ± 7%. The detection limit of the instrument was 0.03 pmol l^{-1} three times the standard deviation of the blank. Certified reference materials ORMS-5 (National Research Council Canada) and ERM-CA400 (European reference materials) were run at the beginning and the end of each measuring session to confirm the precision of our analytical method. Certified concentrations for tHg are 131 ± 6.5 pmol l^{-1} for ORMS-5 and 83.8 ± 5.5 pmol l^{-1} for ERM-CA400. Both CRMs were always within the certified ranges with 131 ± 3.1 pmol l^{-1} ($n = 44$) for ORMS-5 and 83.9 ± 3.5 pmol l^{-1} ($n = 46$) for ERM-CA400. Additional information on the uncertainty of the measurements is given in Supplementary Information 2.

MeHg was measured via a gas chromatography sector field inductively coupled plasma mass spectrometer and quantified by isotopic dilution. Briefly, a subsample of approximately 145 ml was transferred into 160 ml narrow-mouth glass vials (VWR). The glass vials were acid cleaned and muffled at 450 °C for 4 hours before use. The pH of the samples was adjusted to pH 3.9 using a sodium acetate buffer solution (ULTREX II Ultrapure Reagent, J.T. Baker) and NH3 (ULTREX II Ultrapure Reagent, J.T. Baker). Isotopically enriched spikes $i^{199}Hg$ and $MM^{201}Hg$ (ICS) were added to the samples targeting an optimal excess ratio of 4.2 and 5.1, respectively. After 10 minutes of equilibration, a freshly made 5% v/v solution of sodium tetrapropylborate (Merseburger Spezialchemikalien) and 150 µl isooctane (Sigma-Aldrich) were added, and the bottles were sealed with a Teflon-lined crimp cap (Fisherbrand). Samples were shaken for 15 minutes on an orbital shaker (Edmund Buhler KS15). The organic phase containing the derivatized Hg was transferred to vials for injection on a gas chromatography column (GC, THERMO GC 1300 with GC220 transfer module) coupled to a sector field inductively coupled plasma mass spectrometer (SF-ICP-MS, Thermo Element XR) system. The detection limit was 0.001 pmol l^{-1}. Reverse isotopic dilution with Brooks Rand MeHgCl standard traceable to NIST1641E was carried out on the MM201Hg to determine the accuracy of the isotopically labelled spike, as compared to the theoretical concentration of 96.6 ± 7.9%.

The Hg concentration of the rock samples was analysed by cold vapour atomic absorption spectrometry (AAS, LECO AMA 254) according to the US Environmental Protection Agency (EPA) method 7473. Briefly, between 20 to 100 mg of each homogenized sample was introduced into a pre-cleaned nickel vessel. When dried and thermally decomposed, the generated products including Hg were carried away by oxygen flow to the catalytic decomposition tube and purified by the adsorbent. Then the Hg was selectively trapped by gold amalgamation, heated, desorbed and detected by AAS with a low-level optical cell. The instrumental calibration was made with the NIST-3133 certified standard solution and verified daily against the marine sediment certified reference material MESS-4 (certified concentration of 90 ± 40 ng g^{-1}, National Research Council of Canada). The absolute detection limit of Hg was 0.01 ng. Quality assurance and quality control were conducted using method blanks, sample replication and certified reference material (MESS-4). Method blanks were <1% of the Hg mass of the measured samples. The MESS-4 was analysed after every five samples to test for recovery. The reference material was within the certified ranges with 70 ± 2.4 ng g^{-1} ($n = 8$). To confirm the complete release of Hg from the rock samples, the ash product of the thermal decomposition of two samples (Hg concentrations of 734 and 839 ng g^{-1}) was further digested by adding inverse aqua regia and heating at 120 °C for 8 hours. The digested product was measured by cold vapour atomic fluorescence as described above. The Hg concentrations of the ashes after digestion were less than 14 ng g^{-1}, indicating that more than 98% of the Hg is successfully released by the thermal decomposition method.

Calculations

The dilution factor DF_n from the vent site to the buoyant plume was calculated for each depth n using equation (1) as previously defined by many authors[35,44].

$$DF_n = \frac{Mn_{vf} - Mn_o}{Mn_s - Mn_o} \quad (1)$$

Where the subscripts vf, o, and s indicate vent fluid end member, background North Atlantic Ocean seawater concentration, and sample concentration, respectively. The expected concentration of the tracer C_n (tHg, tFe or dFe) at each depth n was calculated using equation (2)[35].

$$C_n = C_o + \frac{1}{DF_n}(C_{vf} - C_o) \quad (2)$$

This expected concentration (C_n) would be the concentration that would be measured if just dilution would account for the losses from the vent site to the plume. Therefore, dilution efficiency is defined as the percentage of the measured tracer (C_s = tHg, tFe or dFe) relative to the expected concentration (C_n) as

$$\text{Dilution efficiency} = \frac{C_s \times 100}{C_n} \quad (3)$$

The volume flux (V) of discharged hydrothermal fluid was calculated using equation (4)[33,35,36].

$$H = \rho \times C_p \times V \times \Delta T \quad (4)$$

Where H is the heat flux reported in the literature, ρ the density of the vent fluid 1,043 kg m^{-3}, C_p the specific heat of hydrothermal fluid at constant pressure 4,100 J kg^{-1} K^{-1} and ΔT the temperature difference between the seawater 2 °C and the hydrothermal fluid 365 °C.

Data availability

Mercury, iron and manganese data for vent fluids, plume, seawater and rock samples are publicly available at https://doi.org/10.6084/m9.figshare.24314527.

References

43. Heimbürger, L. E. et al. Shallow methylmercury production in the marginal sea ice zone of the central Arctic Ocean. *Sci. Rep.* **5**, 10318 (2015).
44. James, R. H. & Elderfield, H. Dissolved and particulate trace metals in hydrothermal plumes at the Mid-Atlantic Ridge. *Geophys. Res. Lett.* **23**, 3499–3502 (1996).
45. Damm, K. L. V. et al. Chemistry of submarine hydrothermal solutions at 21°N, East Pacific Rise. *Geochim. Cosmochim. Acta* **49**, 2197–2220 (1985).
46. Leatherland, T. M., Burton, J. D., McCartney, M. J. & Culkin, F. Mercury in north-eastern Atlantic Ocean water. *Nature* **232**, 112–112 (1971).
47. Mason, R. P., Rolfhus, K. R. & Fitzgerald, W. F. Mercury in the North Atlantic. *Mar. Chem.* **61**, 37–53 (1998).
48. Mason, R. P. & Sullivan, K. A. The distribution and speciation of mercury in the South and equatorial Atlantic. *Deep Sea Res. Part II* **46**, 937–956 (1999).
49. Mason, R. P., Lawson, N. M. & Sheu, G.-R. Mercury in the Atlantic Ocean: factors controlling air–sea exchange of mercury and its distribution in the upper waters. *Deep Sea Res. Part II* **48**, 2829–2853 (2001).
50. Pohl, C. et al. Synoptic transects on the distribution of trace elements (Hg, Pb, Cd, Cu, Ni, Zn, Co, Mn, Fe and Al) in surface waters of the northern and southern East Atlantic. *J. Mar. Syst.* **84**, 28–41 (2011).
51. Bratkič, A. et al. Mercury presence and speciation in the South Atlantic Ocean along the 40° S transect. *Glob. Biogeochem. Cycles* **30**, 105–119 (2016).
52. Canário, J. et al. Mercury and methylmercury in the Atlantic sector of the Southern Ocean. *Deep Sea Res. Part II* **138**, 52–62 (2017).
53. Kütter, V. T. et al. Mercury distribution in water masses of the South Atlantic Ocean (24° S to 20° S), Brazilian Exclusive Economic Zone. *Mar. Pollut. Bull.* **176**, 113425 (2022).

Acknowledgements

This project was supported by the French National Funding Agency project HydrOThermal Mercury (ANR-21-CE34-0026) and the European Union's Horizon 2020 research and innovation programme under the Marie Skłodowska-Curie GMOS-Train, GA grant agreement number 860497. R.S. acknowledges the fund provided by the National Natural Science Foundation of China (42173011). We thank A. Lestari and F. Ni for assisting with the tHg analysis, S. G. Kohler for proofreading and J. Torres Sanabria for the illustrations in Fig. 4. We thank the sampling teams, fellow scientists, crew and captains of the three research expeditions. The HERMINE cruise was funded by the IFREMER REMIMA project. Special thanks to M. Roudaut, V. Guyader, H. Whitby, A. Gourain and T. Holmes for managing the rosette and collecting seawater samples at sea. We are grateful to Y. Fouquet and G. Sarthou for the support.

Author contributions

N.T.-R. contributed to conceptualization, analysis and visualization and wrote the original draft. J.Y. contributed to analysis, writing, reviewing and editing. S.P. contributed to investigation, reviewing and editing. A.D. contributed to analysis and validation. D.G.-S. contributed to reviewing and editing. V.C. contributed to analysis, investigation, validation, reviewing and editing. H.P. contributed to validation, reviewing and editing. M.H. contributed to funding acquisition, reviewing and editing. D.A. contributed to reviewing and editing. C.C. contributed to investigation, reviewing and editing. E.P. contributed to conceptualization, investigation, funding acquisition, reviewing and editing. R.S. contributed to investigation, reviewing and editing. J.E.S. contributed to investigation, reviewing and editing. G.W.L. contributed to investigation, funding acquisition, reviewing and editing. L.E.H.B. contributed to conceptualization, analysis, investigation, resources, funding acquisition, writing, reviewing, editing and supervision.

Competing interests

The authors declare no competing interests.

Additional information

Extended data is available for this paper at https://doi.org/10.1038/s41561-023-01341-w.

Supplementary information The online version contains supplementary material available at https://doi.org/10.1038/s41561-023-01341-w.

Correspondence and requests for materials should be addressed to Natalia Torres-Rodriguez or Lars-Eric Heimbürger-Boavida.

Peer review information *Nature Geoscience* thanks the anonymous reviewers for their contribution to the peer review of this work. Primary Handling Editor: Xujia Jiang, in collaboration with the *Nature Geoscience* team.

https://doi.org/10.1038/s41561-023-01341-w

a

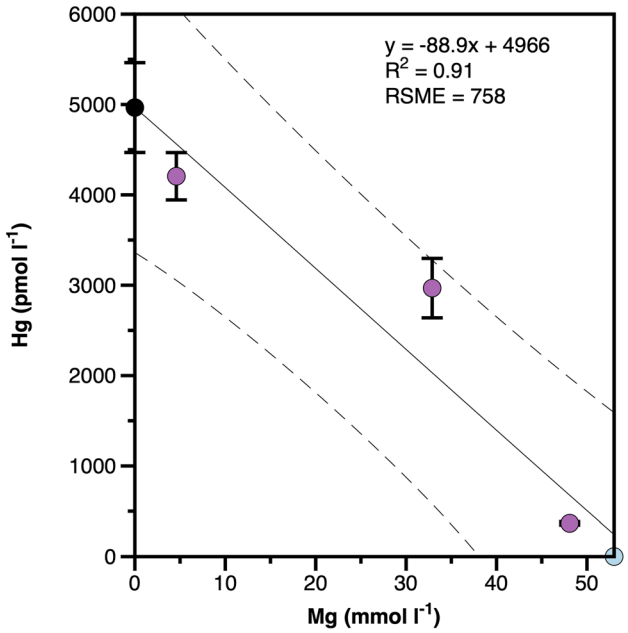

b

Sample ID	Dive	Latitude (°N)	Longitude (°W)	Depth (m)	pH	Temperature (°C)	Mg (mmol l^{-1})	Hg (pmol l^{-1})
Seawater							53**	0.80 ± 0.42 ++
T7	J2-668	26°8.243′	44°49.576′	3619	5.11	347	48.1	367 ± 18
T1	J2-665	26°8.243′	44°49.579′	3621	4.56	303	32.9	2,968 ± 87
T8	J2-668	26°8.234′	44°49.577′	3621	3.01	365	4.59	4,206 ± 262
Vent Fluid end-member							0*	4,966 ± 497+

Extended Data Fig. 1 | Vent fluid end-member estimation. a, least squares estimation of the vent fluid end-member from TAG. Vent fluids samples in purple, seawater in blue, and estimated vent fluid end-member in black. **b**, table with the location of the vent fluids taken at the TAG active mound. *Vent fluid end-member Mg concentration[18].**Seawater Mg concentration[45].+Vent fluid end-member tHg concentration from the least squares calculation.++Seawater Hg concentration median of the Atlantic Ocean without doubtful data[46–53] (see Extended Data Fig. 2).

https://doi.org/10.1038/s41561-023-01341-w

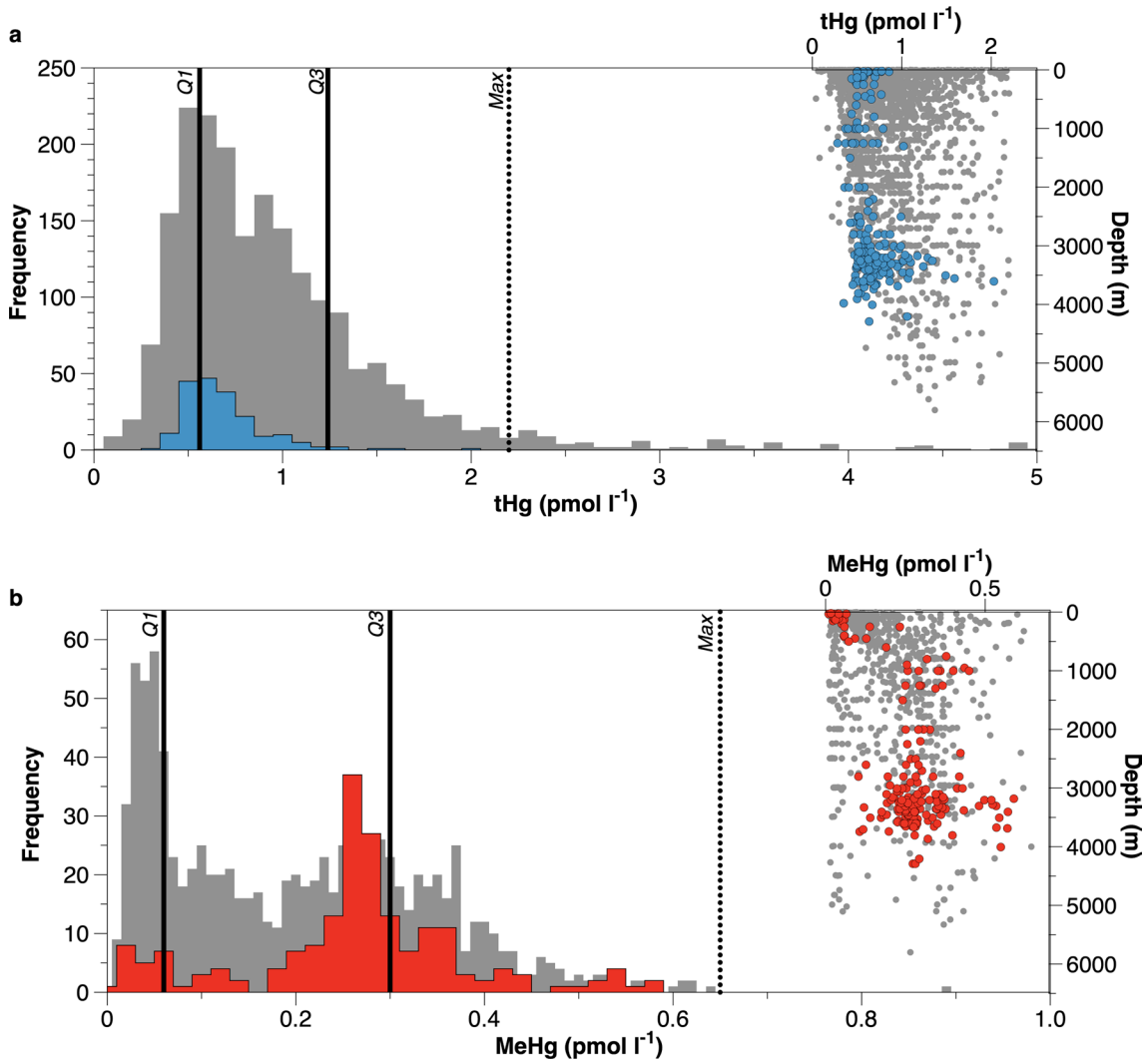

Extended Data Fig. 2 | Atlantic Ocean database statistics and comparison with the present study. a, Histogram showing the distribution of tHg data for the Atlantic Ocean in grey and this study tHg in blue. **b**, Histogram showing the distribution of MeHg data for the Atlantic Ocean in grey and this study MeHg in red. Statistical parameters Q1, Q3, and maximum value (Max) are shown with vertical lines in both histograms. The maximum value is determined as 1.5 times the interquartile range. Data points beyond are considered outliers. In the right part of the histograms a comparison between this study data and the Atlantic Ocean without outliers.

https://doi.org/10.1038/s41561-023-01341-w

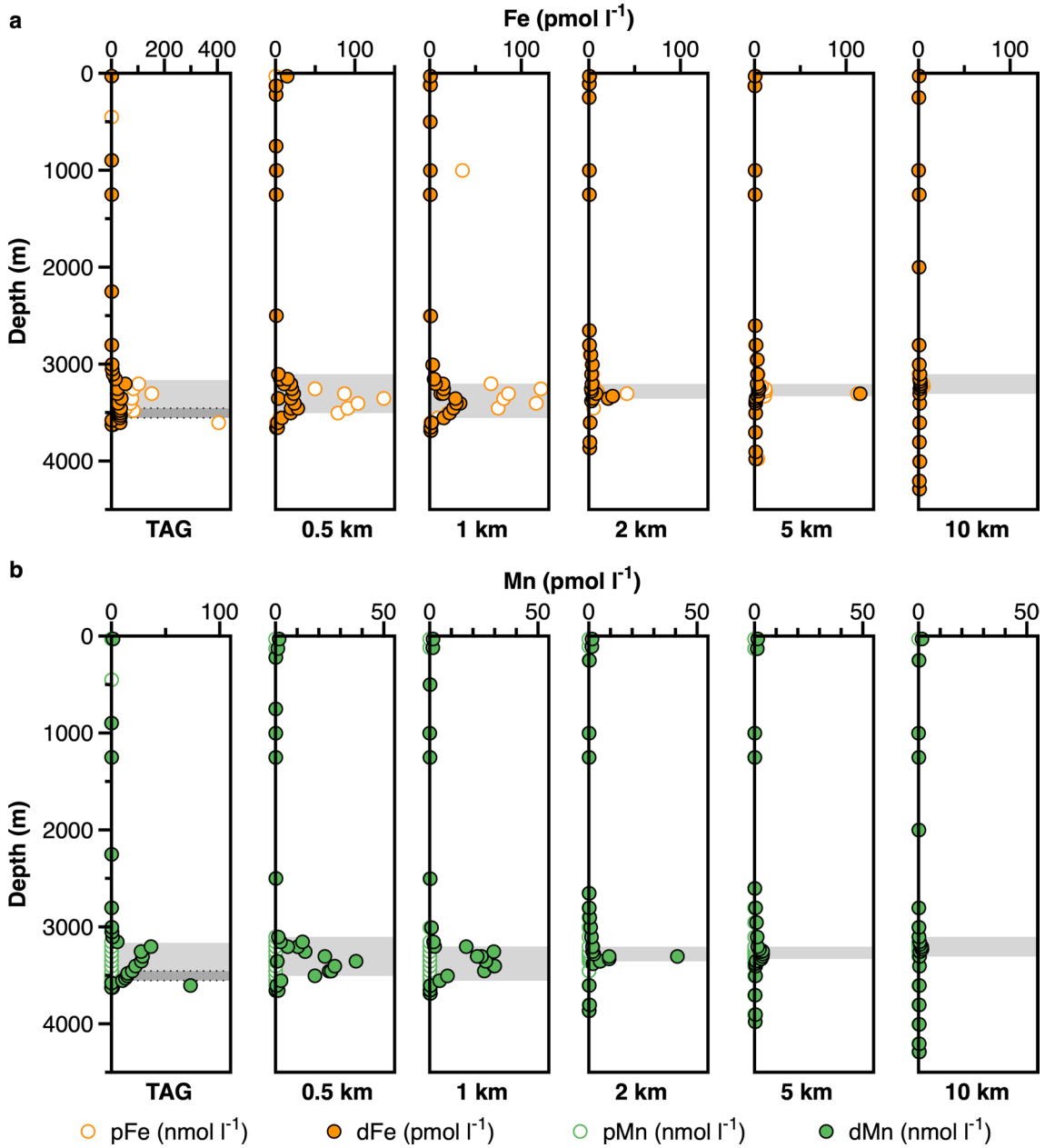

Extended Data Fig. 3 | Vertical profiles of Fe and Mn. a, Vertical profiles for Fe. **b**, Vertical profiles for Mn. Note the change of scale between the TAG and the other stations[19].

https://doi.org/10.1038/s41561-023-01341-w

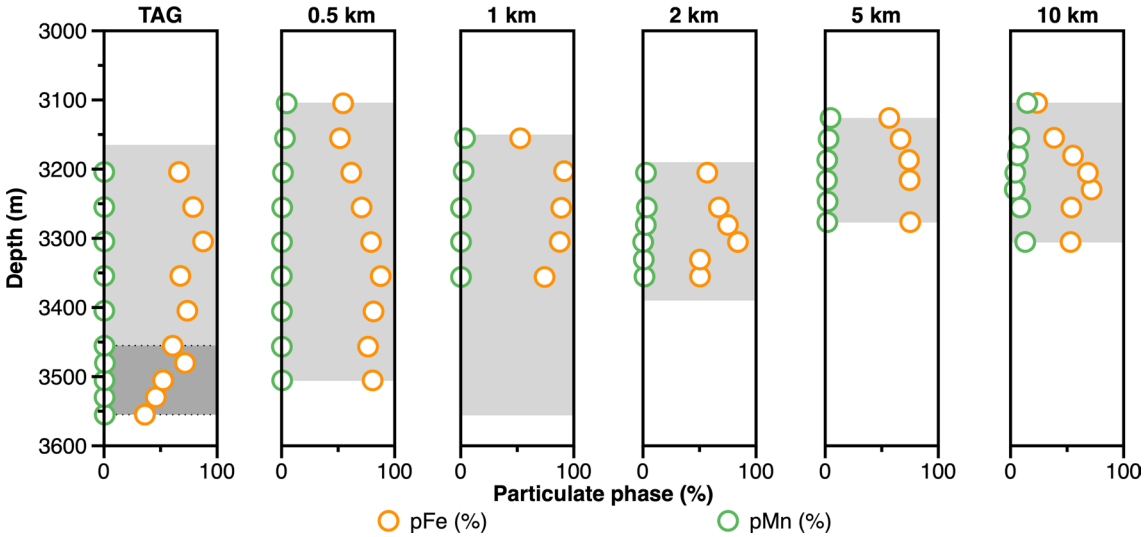

Extended Data Fig. 4 | Percentage of pFe and pMn phases. Note the low percentages of pMn in all the stations and depths. Considering all stations and depths within the plume pMn accounts for 2.5% of the tMn and pFe accounts for 66% of the tFe[19].

https://doi.org/10.1038/s41561-023-01341-w

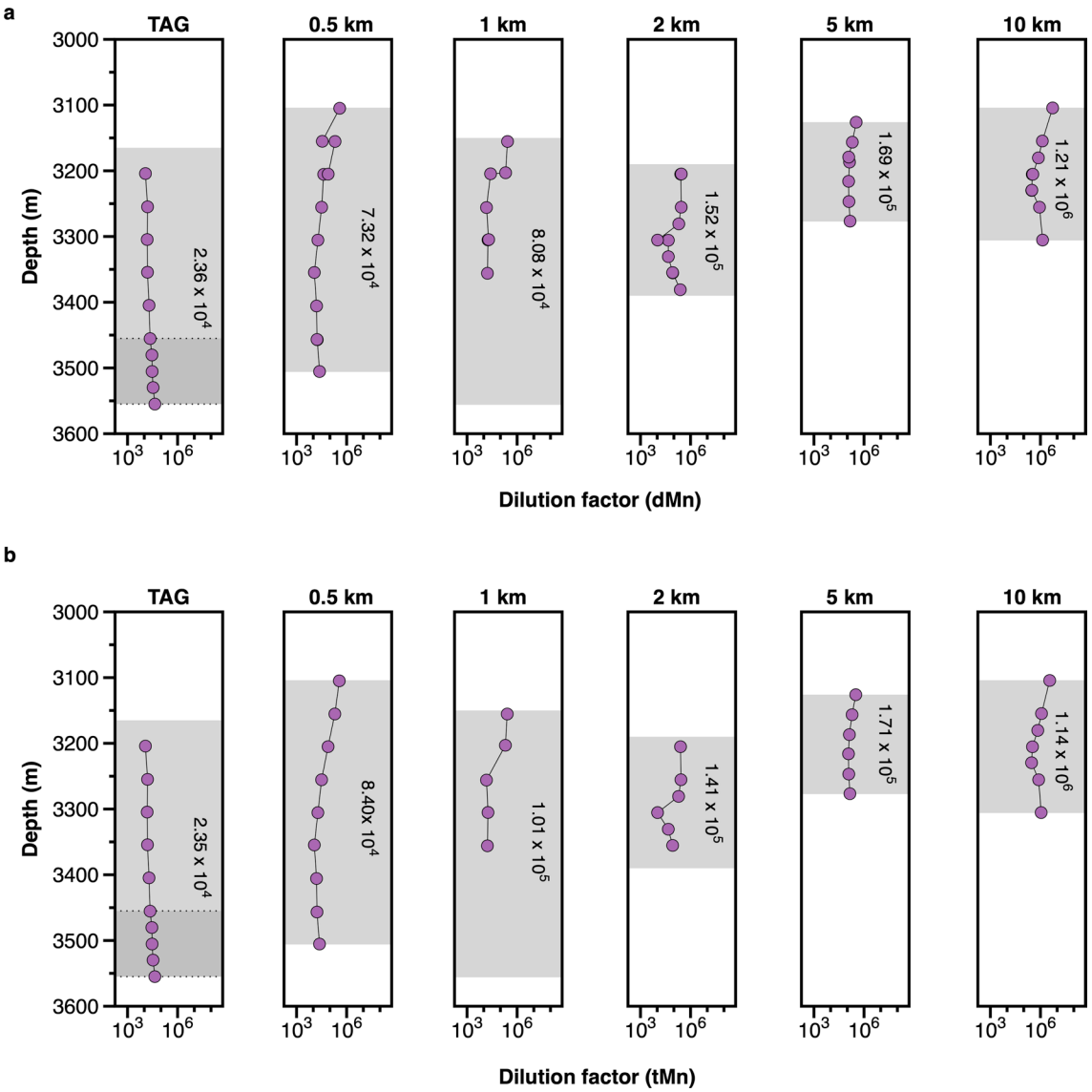

Extended Data Fig. 5 | Calculated dilution factor at different stations along the plume. a, dilution factors calculated using dMn concentrations in the plume. **b**, dilution factors calculated using tMn concentrations in the plume.

https://doi.org/10.1038/s41561-023-01341-w

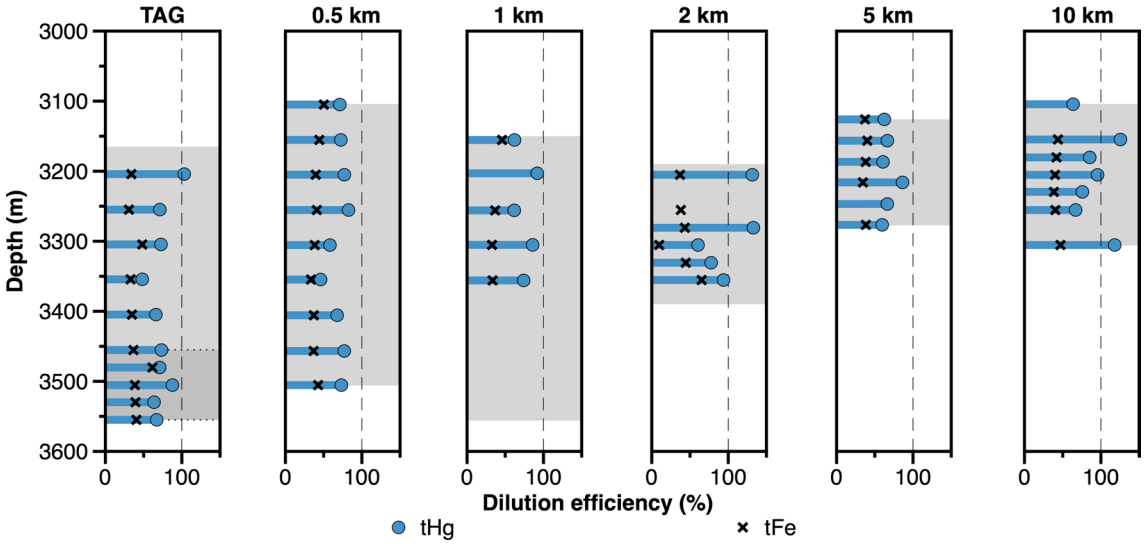

Extended Data Fig. 6 | Dilution efficiency at different stations and depths. In blue tHg dilution efficiency. Black crosses indicate tFe dilution efficiency. The grey shading shows the non-buoyant plume depth. Dotted lines and darker shading at the TAG station bound the depths of the buoyant plume. Note that in this figure the tFe is plotted instead of dFe plotted in Fig. 2 in the main text.

https://doi.org/10.1038/s41561-023-01341-w

Extended Data Table 1 | Reported tHg and MeHg concentrations in the Atlantic Ocean in comparison with data reported in the present study

Study	Ref	tHg (pmol l^{-1})	mean tHg (pmol l^{-1})	median tHg (pmol l^{-1})	tHg (n)	tHg SD	MeHg (pmol l^{-1})	mean MeHg (pmol l^{-1})	median MeHg (pmol l^{-1})	MeHg (n)	MeHg SD
Leatherland et al. 1971+	46	14.9 - 99.7	66.5	74.8	9	27.7	-	-	-	0	
Carr et al. 1974+	14	4,337 - 7,079	5,434	5,434	15	964	-	-	-	0	
Carr et al. 1975+	15	334 - 5,384	2,050	818	32	2400	-	-	-	0	
Mason et al. 1998	47	0.63 - 7.23	2.35	1.76	27	1.62	-	-	-	0	
Mason & Sullivan. 1999	48	0.59 - 13.3	2.46	1.81	59	2.49	-	-	-	0	
Mason et al. 2001	49	0.30 - 6.74	1.50	1.13	37	1.29	-	-	-	0	
Pohl et al. 2011	50	0.46 - 4.90	1.89	1.68	64	1.05	-	-	-	0	
Bowman et al. 2015*	17	0.04 - 12.8	0.92	0.89	649	0.59	0.02 - 0.89	0.23	0.21	222	0.15
Bratkic et al. 2016	51	0.40 - 5.73	1.42	1.35	375	0.60	0.01 - 0.24	0.04	0.04	126	0.03
Canario et al. 2017	52	0.10 - 3.61	0.89	0.71	46	0.71	0.02 - 0.56	0.17	0.15	47	0.12
Cossa et al. 2018**	22	0.07 - 1.65	0.57	0.53	552	0.20	0.03 - 0.61	0.21	0.19	450	0.13
Kütter et al. 2022+	53	4.4 - 10.6	5.96	5.90	38	1.13	-	-	-	0	
This study		0.28 - 2.03	0.68	0.63	195	0.23	0.01 - 0.60	0.26	0.27	192	0.12
Atlantic Ocean all data		0.04 - 5,384	7.59	0.85	2070	482	0.01 - 0.89	0.20	0.19	1036	0.14
Atlantic Ocean without outliers+		0.04 - 13.34	1.00	0.80	1917	0.42					

*Methylmercury (MeHg) as the sum of monomethylmercury (MMHg) and dimethylmercury (DMHg).
**MeHg data available on GEOTRACES intermediate data product (link).
+Doubtful data (see **Extended data Fig. 2**).

https://doi.org/10.1038/s41561-023-01341-w

Extended Data Table 2 | Lithology and Hg concentrations of surface rock samples at TAG

Number in Fig. 3	Zone I	Sample ID	Latitude (°N)	Longitude (°W)	Type	Hg (ng g^{-1})
1	Surface	ALV2190-8-1	26° 08.22'	44° 49.56'	Massive granular pyrite	121
2		ALV2190-12-1	26° 08.19'	44° 49.55'	Red ocher	74
3		ALV2583-3	26° 08.24'	44° 49.58'	Fe oxides with relict sulfides	99
4		ALV2587-1	26° 08.23'	44° 48.46'	Nodular pyrite breccia with minor anhydrite	341
5		ALV2588-1	26° 08.23'	44° 49.59'	Porous Fe oxyhydroxide chimney	409
6		ALV2586-3	26° 08.47'	44° 48.46'	Mn iron oxyhydroxides	103
Black dotted line		Sulfides at mid-ocean ridges [31]			Massive sulfides	2,000
Black dotted line		Oceanic crust [30]				10

https://doi.org/10.1038/s41561-023-01341-w

Extended Data Table 3 | Lithology, sample location, depth, and Hg concentrations of the drill-core samples

Number in Fig. 3	Zone I	Zone	Sample	Lithology	Area	Latitude (°N)	Longitude (°W)	Depth (mbsf)	Hg (ng g^{-1})
7	Massive sulfide	Massive Sulfide	957H 1N1/14	porous nodular pyrite breccia	TAG2	26° 08.195'	44° 49.555'	9	99.9
8		Massive Sulfide	957P 6R1/3	nodular pyrite breccia	TAG5	26° 08.236'	44° 49.558'	27	101
9		Massive Sulfide	957F 2N1/4	massive granular pyrite	TAG1	26° 08.202'	44° 49.564''	6	163
10		Massive Sulfide	957M 2R1/5	porous massive pyrite	TAG4	26° 08.222'	44° 49.588	10	949
11		Massive Sulfide	957A 3X1/1	chert sulfide breccia	TAG2	26° 08.196'	44° 49.552''	9	1,021
12		Massive Sulfide	957I 1N1/3	porous massive pyrite	TAG4	26° 08.226'	44° 49.585	9	1,187
13	Stockwork	Anhydrite rich	957C 7N2/1B	nodular siliceous pyrite-anhydrite breccia	TAG1	26° 08.226'	44° 49.555'	21	50.4
14		Pyrite silica	957C 13N2/3C	pyrite-silica breccia	TAG1	26° 08.226'	44° 49.555'	39	237
15		silicified wallrock breccia	957E 12R1/5	silicified wallrock breccia	TAG1	26° 08.219'	44° 49.560'	92	78.4
16		silicified wallrock breccia	957H 5N2/1C	silicified wallrock breccia	TAG2	26° 08.195'	44° 49.555'	28	81.4
17		silicified wallrock breccia	957C 15N3/7	silicified wallrock breccia	TAG1	26° 08.226'	44° 49.555'	45	90.1
18		silicified wallrock breccia	957E 10R1/2	massive granular pyrite	TAG1	26° 08.219'	44° 49.560'	82	320
19		silicified wallrock breccia	957E 9R1/1	massive granular pyrite	TAG1	26° 08.219'	44° 49.560'	78	331

https://doi.org/10.1038/s41561-023-01341-w

Extended Data Table 4 | Calculation of the Hg in the TAG deposit and the Hg flux

		Rock (t)	Ref	Hg samples av (ng g^{-1})	Hg entire layer (t)
Part 1	Massive sulfide layer	2,270,000	32	1,021 ± 122	2.32
	Stockwork zone	680,000		90 ± 123	0.06
	TAG active mound deposit	2,950,000			2.38

		Heat Flux (MW)	Ref	Volume flux (m^3 s^{-1})	Hg flux (g y^{-1})
Part 2	TAG Active Mound	225	34	0.14	4,553
		55-86	33	0.04	1,113

		Active time (y)	Ref	Hg flux (g y^{-1})	Hg release (t)
Part 3	TAG Active Mound	20,000	37	4,553	91.1
				1,113	22.3

		Ref	Hydrothermal vents flux (kg y^{-1})	Ref	Hydrothermal vents Hg flux (kg y^{-1})	Hydrothermal vents Hg flux (t y^{-1})
Part 4	Vent fluid end-member 4,966 ± 497 pmol l^{-1}	This study	1.70E+12	38	1,524	1.5
			2.93E+13		32,108	32.1
	Highest reported vent fluid end-member 11,000 pmol l^{-1}	10	2.93E+13		64,650	64.7

		Ref	Hg flux (t y^{-1})	Anthropogenic Hg flux (to the ocean) (t y^{-1})	Natural Hg flux (to the ocean) (t y^{-1})	Natural Hg (%) from anthropogenic
Part 5	Atmospheric deposition (to the ocean)	39	4,300 – 7,800	4,755 – 8,789	236.5 - 499.7	3 - 11
	Riverine discharge (to the ocean)	40	893 – 1,224			
	Terrestrial geogenic sources (to the atmosphere)	41	235 – 435 (335 ± 100)			